Materials Science and Engineering A 547 (2012) 19–31

Contents lists available at SciVerse ScienceDirect

Materials Science and Engineering A

journal homepage: www.elsevier.com/locate/msea

Experimental and numerical study of dynamic strain ageing and its relation to ductile fracture of a C–Mn steel

H.D. Wang[a,b], C. Berdin[a,c,*], M. Mazière[d], S. Forest[d], C. Prioul[a], A. Parrot[b], P. Le-Delliou[b]

[a] Laboratoire de Mécanique Sols, Structures et Matériaux, CNRS UMR 8579, Grande Voie des Vignes, 92290 Châtenay-Malabry, France
[b] Electricité de France, R&D Division, Département MMC, Les Renardières, 77818 Moret-sur-Loing, France
[c] University Paris-Sud 11, ICMMO/LEMHE CNRS UMR 8182, 91400 Orsay, France
[d] Centre des Matériaux, Mines ParisTech, CNRS UMR 7633, BP 87, F-91003 Evry cedex, France

ARTICLE INFO

Article history:
Received 24 November 2011
Received in revised form 6 March 2012
Accepted 8 March 2012
Available online 29 March 2012

Keywords:
Dynamic strain ageing
Ductile fracture
Numerical modeling
Strain localization
Local approach

ABSTRACT

Ductile fracture of a C–Mn steel was characterized by tensile tests performed in a large temperature range (from 20 to 350 °C) on round notched and CT specimens. The experimental results revealed a sharp decrease in fracture strain and fracture toughness around 200 °C. These temperatures correspond to the domain of dynamic strain ageing (DSA). The Portevin-Le Chatelier (PLC) effect, which is the most classical manifestation of DSA, was simulated for round notched and CT specimens with a mechanical constitutive model which includes the strain ageing effect and the stiffness of the testing machine. It is shown that changes in stiffness can amplify the DSA effect. 3D-Modeling was used to correctly capture the complex space-time correlation of strain localization, particularly in side-grooved CT specimens. The results were compared to classical elastic–plastic simulations. The local approach to fracture was then applied to predict the ductile fracture of round notched specimens using the Rice and Tracey criterion. In the DSA domain, the approach used in this study predicts a decrease of the fracture strain which is less than observed experimentally.

1. Introduction

The dynamic strain ageing (DSA) effect can occur in many metal alloys. This phenomenon is due to the interaction between solute atoms and mobile dislocations [1,2] during straining. DSA reduces the strain rate sensitivity of the flow stress and induces a jerky flow when the strain rate sensitivity becomes negative [3]. In such a case, strain localizes into narrow bands inducing stress drops on the overall stress–strain curve [4,5] usually referred to as "serrations". This phenomenon is called the "Portevin-Le Chatelier (PLC)" effect. Dynamic strain ageing occurs for temperatures and strain rates within a certain range, and in some cases a critical strain level has to be reached for serrated yielding to take place [3,6].

Dynamic strain ageing and the PLC effect have been the subjects of numerous experimental and theoretical studies. In the past decade, numerical modeling with the finite element (FE) method has also been used to investigate the PLC effect and related phenomena. These studies have been aimed at representing the spatio-temporal evolution of the local mechanical variables using appropriate constitutive laws. McCormick and Ling [7] proposed a model derived from the approach proposed by McCormick [6], Estrin and McCormick [8] and McCormick and Estrin [9] to simulate the PLC effect. Typical characteristics of the PLC effect, such as PLC instabilities and critical plastic strain, were correctly predicted with this model. Zhang et al. [10] adapted the McCormick and Ling [7] model, an elasto-viscoplastic constitutive law accounting for DSA through a new internal variable, the ageing time t_a and a hardening term. The morphology of PLC bands in Al–Mg–Si alloys was then studied via FE analysis using this model. Kok et al. [11,12] used a polycrystal plasticity model embedded in a FE framework to study the PLC effect in constant cross head velocity controlled tension tests. These authors used a constitutive law based on the Zhang et al. [10] model and introduced the model into a law of crystalline plasticity. Graff et al. [13,14] reformulated the constitutive model of Zhang et al. [10] through the introduction of a thermally activated elasto-viscoplastic law. This formulation was used by Belotteau et al. [15] to predict strain ageing (both static and dynamic) of a C–Mn steel over a large range of temperatures and strain rates. Mazière et al. [16] used the same constitutive model to simulate round smooth and notched specimens of a Ni based superalloy. Benallal et al. [17] used a phenomenological elastic–viscoplastic model based on [1] to study the PLC effect in tension tests with smooth axisymmetric specimens at different strain rates and with U-notched axisymmetric specimens. The experimental results,

* Corresponding author at: Université Paris-Sud 11, ICMMO/LEMHE CNRS UMR 8182, bat 410, 91405 Orsay cedex, France. Tel.: +33 1 69 15 31 97; fax: +33 1 69 15 48 19.
E-mail address: clotilde.berdin@u-psud.fr (C. Berdin).

0921-5093/$ – see front matter © 2012 Elsevier B.V. All rights reserved.
http://dx.doi.org/10.1016/j.msea.2012.03.069

presented in a previous paper [18], were correctly predicted by the approach proposed in [17]. For example, the authors used different strain hardening laws for different strain rates to simulate negative strain rate sensitivity and were able to predict strain localization bands (PLC bands) using this model. Hopperstad et al. [19] used an anisotropic elastic–viscoplastic model including the McCormick model [6,10,20] for DSA. One can find an exhaustive critical review of existing numerical models which predict DSA and PLC effects in Rizzi and Hahner [21]. In addition, PLC effects in notched and cracked specimens were numerically investigated by Graff et al. [13,14] and Belotteau et al. [15] with 2D models. Recently, a 3D model of a notched CT specimen was used to study the strain localization stemming from static ageing including residual stress and plastic strain obtained by preloading in compression [22].

DSA is characterized by an increase in flow stress and ultimate tensile strength but also by a drop in fracture toughness [15,23–25]. However, Srinivas et al. [26,27] found the opposite effect of DSA on fracture toughness in a pure Armco Iron. The authors attributed this behavior to the absence of inclusions in pure iron which modifies the underlying ductile fracture mechanisms in the presence of DSA. Carbon–manganese steels, used for the secondary systems (feed water line and steam line) of nuclear pressurized water reactors, are sensitive to DSA at in-service temperatures (around 200 °C) [15,24]. Therefore, the design of these components requires the prediction of fracture toughness of these steels in the presence of DSA.

Amar and Pineau [28] and Wagner et al. [24] modelled the ductile fracture of such C–Mn steels in the presence of DSA. They used an elastic–plastic constitutive law ignoring the DSA effect. To predict the drop in fracture toughness, they applied the Rice and Tracey criterion [29]. So, a critical void growth ratio was identified at each temperature on notched tensile tests results. The results showed a variation in critical void growth ratio, which, however, was not evidenced on fracture surface [24]. Indeed, DSA can modify the local mechanical variables, especially when strain rate sensitivity is negative: strain localizations occur even in notched specimens that could induce a modification of the damage kinetics rather than a modification of the critical value.

Thus, the objective of the present study is to model the mechanical behaviour with an elasto-viscoplastic constitutive law which accounts for DSA and to predict, using a local approach, the fracture of a C–Mn steel in the DSA domain particularly at 200 °C. Consequently, the tensile behaviour is studied and modeled using a model derived from Kubin, McCormick, Estrin's works [3,6]. The fracture behavior of one C–Mn steel is characterized using notched tensile and precracked tests. Finite element simulations of fracture tests are performed taking DSA into account. These simulations are carried out in 2D but also in full 3D. Finally, the Rice and Tracey [29] criterion is applied to predict the fracture in the presence of DSA.

2. Experimental tests

2.1. Tensile tests

The material studied is a carbon manganese steel which was used by Belotteau et al. [15]. Mechanical behavior of the material was characterized by fourteen tensile tests performed on round tensile specimens (36 mm gage length, 6 mm diameter) at seven temperatures over the temperature range (20–350 °C) and at two strain rates: $10^{-2}\,s^{-1}$ and $10^{-4}\,s^{-1}$. Additional tests at two other strain rates were performed: $10^{-3}\,s^{-1}$ and $10^{-5}\,s^{-1}$ in order to improve the accuracy of the constitutive model [30] presented below. The PLC effect occurred in the temperature range of 150–300 °C, depending on the strain rate. Table 1 shows the per cent uniform elongation (A_u) for round tensile specimens tested at one of the prescribed strain rates ($10^{-3}\,s^{-1}$) for different temperatures.

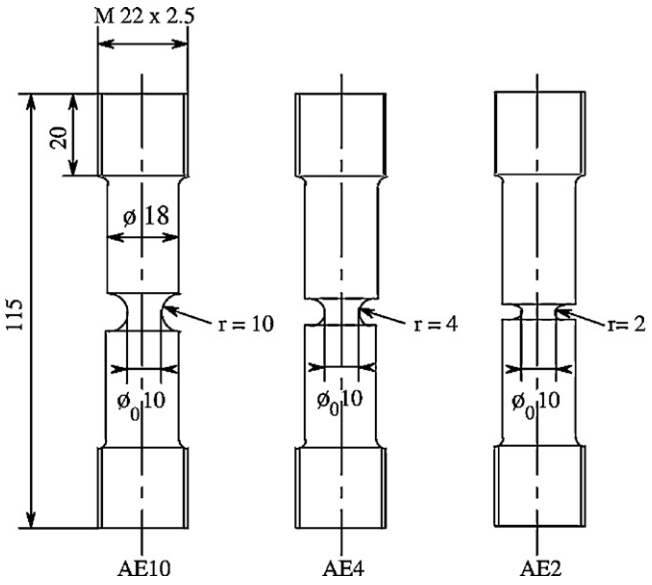

Fig. 1. Round notched specimens (all dimensions are in mm).

There is a minimum in the uniform elongation around 200 °C. The decrease of ductility is correlated with DSA [15,23–25]. The uniform elongation was a minimum at 200 °C for the strain rate of $10^{-4}\,s^{-1}$ and at 250 °C for the strain rate of $10^{-2}\,s^{-1}$ [15]. This behavior is expected since the DSA temperature domain depends on the strain rates; the DSA temperature domain moves to higher temperatures if strain rates increase and vice versa [31].

According to Kang et al. [32], PLC bands provide an additional local strain that enables the Considère condition to be reached locally before it is reached over the whole specimen. This may explain the reduced ductility of tensile specimens in the DSA temperature domain. Indeed, Hosford and Caddell [33] showed that in uniaxial tension, the cross-section inhomogeneity has an important influence on the necking strain. A PLC band may contain 1.4% plastic strain [34] which creates a local cross-section inhomogeneity thus reducing the necking strain. Wang et al. [30] predicted necking within a PLC band on round smooth specimens. Fracture under tension is thus essentially a strain localization problem, because ductile damage occurs after necking. So, tensile elongation does not depend on usual ductile fracture mechanisms. Fracture tests with stress triaxiality ratio promoting ductile damage were then conducted.

2.2. Fracture tests

Tests on round notched specimens were carried out over the same temperature range. The minimum diameter Φ_0 in the notch section was 10 mm for all samples, but the root notch radius r varied from 2 mm (AE2), 4 mm (AE4) and up to 10 mm (AE10) (Fig. 1). Thus, the stress triaxiality ratio, important for ductile fracture, varies between 0.8 and 1.2. To obtain the PLC effect in these tests, strain rates in the range of 10^{-4}-$10^{-3}\,s^{-1}$ have to be reached in the minimum cross-section. Preliminary FE computations allowed us to calculate the crosshead velocity of the testing machine to obtain these strain rates.

During the tensile tests, the variations of the load P versus diameter Φ, measured at the minimum section, were recorded. From these values, the mean stress $\bar{\sigma} = 4P/\pi\Phi_0^2$ and the mean strain $\bar{\varepsilon} = 2\ln(\Phi_0/\Phi)$ were calculated. The mean stress and strain at failure ($\bar{\sigma}_R$ and $\bar{\varepsilon}_R$ respectively) were determined ($\bar{\sigma}_R$ from final diameter Φ_R measured on broken specimens). The results showed that at 200 °C, the PLC effect occurred in the form of serrations

Table 1
Uniform elongation (Au) for round smooth specimens tested at 10^{-3} s^{-1}.

Temperature (°C)	20	100	150	200	250	300	350
Au (%)	20	19.8	19.5	11.8	14.1	15.1	16.1

on the global curve: so, jerky flow behavior is observed not only on smooth tensile specimens, but also on notched specimens. At 200 °C, jerky flow is observed for all geometries.

Table 2 shows the fracture strain $\bar{\varepsilon}_R$ variation with temperature for specimens AE2, AE4 and AE10 and a sharp drop of the fracture strain $\bar{\varepsilon}_R$ is seen in contrast to the usual case, in which the fracture strain is expected to increase with temperature as seen for temperatures above 250 °C.

Tearing tests on CT specimens were carried out over the same temperature range as for the round notched specimens. The specimens used are side-grooved CT25 with an over-all thickness of 25 mm and a reduced thickness of 20 mm at the side grooves. The specimens were fatigue pre-cracked for 1,330,000 cycles at a maximum load of 14,000 N to a pre-crack length of 5 mm corresponding to an over-all initial crack length of 30 mm. At the end of fatigue pre-cracking, the stress intensity factor was $K_I = 20\,\text{MPa}\sqrt{m}$. To calculate the tearing resistance, the specimen unloading compliance method was applied: crack growth was estimated from the unloading compliance at various crack opening displacements (COD). The compliance was calculated assuming a straight crack front under plane strain constraint. The tests were conducted at a prescribed crack opening displacement rate of 0.4 mm/min using a crack clip gauge and stopped when the COD reached 5 mm.

Fig. 2 shows the resistance to ductile fracture for CT specimens as a function of temperature. There was a sharp drop of the initiation fracture toughness, $J_{0.2}$ and of the tearing modulus, dJ/da between 150 and 250 °C due to the DSA effect, as was also observed by Amar and Pineau [28] and Wagner et al. [24] on other C–Mn steels. The reductions of the fracture toughness and tearing modulus from 20 °C to 200 °C were about 60%. Finally, experimental results from notched tensile and CT specimens obtained by Wagner et al. [24] were in agreement with the present results except that the ductility and fracture toughness of the current C–Mn steel was higher.

2.3. Fractographic analysis

To understand the mechanisms of fracture in the presence of DSA, fractographic analyses by SEM (Scanning Electron Microscopy) of broken specimens were carried out. On the fracture surface of AE specimen, no special dimple features were found either in the absence or presence of the PLC effect in agreement with Wagner et al. [24] and Bréchet and Louchet [35]. Other authors [28,36,37] have reported shallower dimples associated with DSA, but these observations were not quantified.

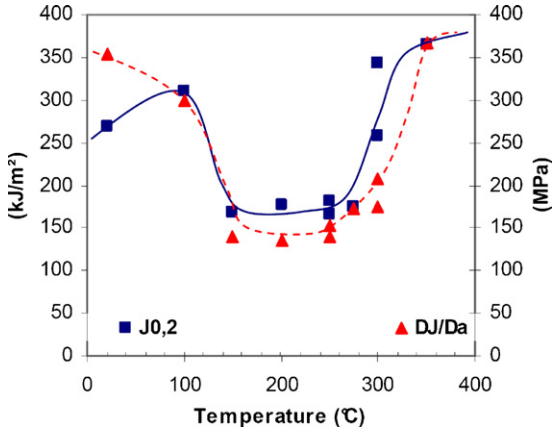

Fig. 2. Evolution of the toughness for CT specimens.

Fig. 3 shows the fractographic analysis on the surfaces of the CT specimens tested at 20 °C (without DSA) and 200 °C (with DSA). The voids are rather spherical and regular with different sizes. The smaller voids were attributed to carbide fracture in pearlite whereas the larger ones were related to the MnS inclusions. Special local flat regions (Fig. 3b) were seen on the specimen fractured at 200 °C: these regions appear to be sheared. However, these areas were rare and not representative of the global fracture surface of the specimen tested at 200 °C. Similar flat regions were also seen by Gupta et al. [38]. These regions could be due to the presence of strain localizations at the crack tip associated to the PLC effect, or to small unstable crack extensions due to local softening as reported by Marshall et al. [39]. However, these infrequent features do not explain the relationship between the DSA effect and the loss of toughness. Mechanical modeling of strain localization was carried out in order to gain further insight into the relationship between DSA and ductile fracture as described below.

3. Numerical modeling

3.1. Constitutive model

In order to model the PLC phenomenon, the KEMC (Kubin–Estrin–McCormick) strain ageing model was invoked. This model incorporates elasto-viscoplastic behavior and thermal activation and was derived from earlier models proposed by Kubin and Estrin [3] and McCormick [6]; it allows the prediction of both types of strain ageing: static strain ageing (SSA) (Lüders effect) and DSA (PLC effect). It was first proposed by Zhang et al. [10] and adapted by Graff et al. [13]. The yield function f is based on the von Mises criterion with isotropic hardening:

$$\begin{aligned} f(\underset{\sim}{\sigma}, R, R_a) &= J_2(\underset{\sim}{\sigma}) - R - R_a \\ R(p) &= Q(1 - \exp(-bp)) + Hp \end{aligned} \tag{1}$$

where Q, b, H are the strain hardening parameters and p is the cumulative equivalent plastic strain. The term $J_2(\underset{\sim}{\sigma})$ represents the second invariant of the deviatoric stress tensor and R is the isotropic strain hardening. Of particular interest in the KEMC model is the introduction of the term R_a which represents the overhardening due to strain ageing:

$$R_a(t_a, p) = P_1 C_s(t_a, p) \tag{2}$$

where C_s defines the relative concentration of solute atoms pinning the mobile dislocations. The parameter P_1 represents the maximal stress drop magnitude from a fully pinned state to a fully unpinned state. The solute atoms concentration depends on the ageing time t_a where higher values of t_a induce stronger overhardening. The variable p is the cumulative equivalent plastic strain:

$$\dot{p} = \sqrt{\frac{2}{3}\dot{\underset{\sim}{\varepsilon}}^p : \dot{\underset{\sim}{\varepsilon}}^p} \quad \dot{\underset{\sim}{\varepsilon}}^p = \dot{p}\frac{3}{2}\frac{\underset{\sim}{\sigma}^{dev}}{J_2(\underset{\sim}{\sigma})} \quad \dot{p} = \dot{\varepsilon}_0 \exp\left(-\frac{E_a}{k_B T}\right) \sinh\left(\frac{\text{Max}(0, f(\underset{\sim}{\sigma}, R, R_a))}{k_B T}\right) \tag{3}$$

where $\underset{\sim}{\varepsilon}^p$ is the plastic strain tensor, $\dot{\varepsilon}_0$, E_a, V_a, k_B, T are the strain rate threshold, the energy and volume of activation of the

Table 2
Evolution of the strain to fracture for round notched specimens.

Temperature (°C)	20	100	125	150	200	250	300	350
AE2	0.543				0.421	0.368		0.474
AE4	0.648	0.580	0.528	0.414	0.404	0.327	0.447	0.528
AE10	0.713				0.441	0.430		0.473

dislocation mobility, the Boltzmann constant and the absolute temperature respectively.

The mean concentration of solute atoms depends on the parameters P_2, α and n:

$$C_s(p, t_a) = C_m(1 - \exp(-P_2 p^{\alpha} t_a^n)) \quad (4)$$

The relative solute concentration evolves to a saturation value C_m when the ageing time t_a tends to infinity. The evolution law of the ageing time depends on the plastic strain rate through a parameter ω which represents the strain increment produced when all arrested dislocations overcome local obstacles and advance to the next pinned configuration (Eq. (5)):

$$\dot{t}_a = 1 - \frac{\dot{p}}{\omega} t_a \quad t_a(t = 0) = t_{a0} \quad (5)$$

The initial time t_{a0} is related to the presence of static ageing and a large value allows simulating the Lüders peak and plateau.

The KEMC model was implemented in FE software [13,16]. The procedure for the parameter identification is explained in detail in [15]. However, some parameters were modified in order to better simulate the serrations and the geometrical features of PLC bands [30]. Here, only the results obtained at 20 °C and at 200 °C are presented and the parameters at these temperatures are provided in Table 3. The simulations were performed with finite strain formulation using the corotational frame of reference [16]. A full implicit resolution solver is used for the global equations. Local integration is solved by the Runge-Kutta method. Since the serrations have to be captured, the time increment is usually very small making the computation time be very large (up to 60,000 increments currently used [15]).

3.2. Smooth tensile specimens

The tests on smooth tensile specimens were first simulated in 2D plane stress in order to minimize computation time. Eight node quadratic elements with reduced integration were employed. Fig. 4 shows a comparison of numerical and experimental tensile curves for two different temperatures at 10^{-3} s^{-1}. As can be seen, the KEMC model simulates both strain ageing phenomena: SSA (Lüders stress peak and plateau and Lüders bands [40]) and DSA (serrated flow and PLC bands). It should be noted that the simulated Lüders plateau is lower than the experimental one. Indeed it is difficult to correctly simulate both static and dynamic strain ageing with this model as previously discussed [15].

3.3. Round notched specimens

Round notched specimens were simulated using the KEMC model with the parameters identified in the previous section. 2D-Axisymmetric and full 3D computations were performed (Fig. 5). Generally, tensile tests on round notched specimens were modeled with a 2D axisymmetric model and planar symmetry: half-section is then modeled. However, in the presence of DSA effect, strain localization bands could occur and these bands present probably neither axisymmetry nor planar symmetry. Indeed, Graff et al. [13] showed, by in situ observations on polished surfaces of the specimens, that PLC bands on U-notched plate tensile specimens were

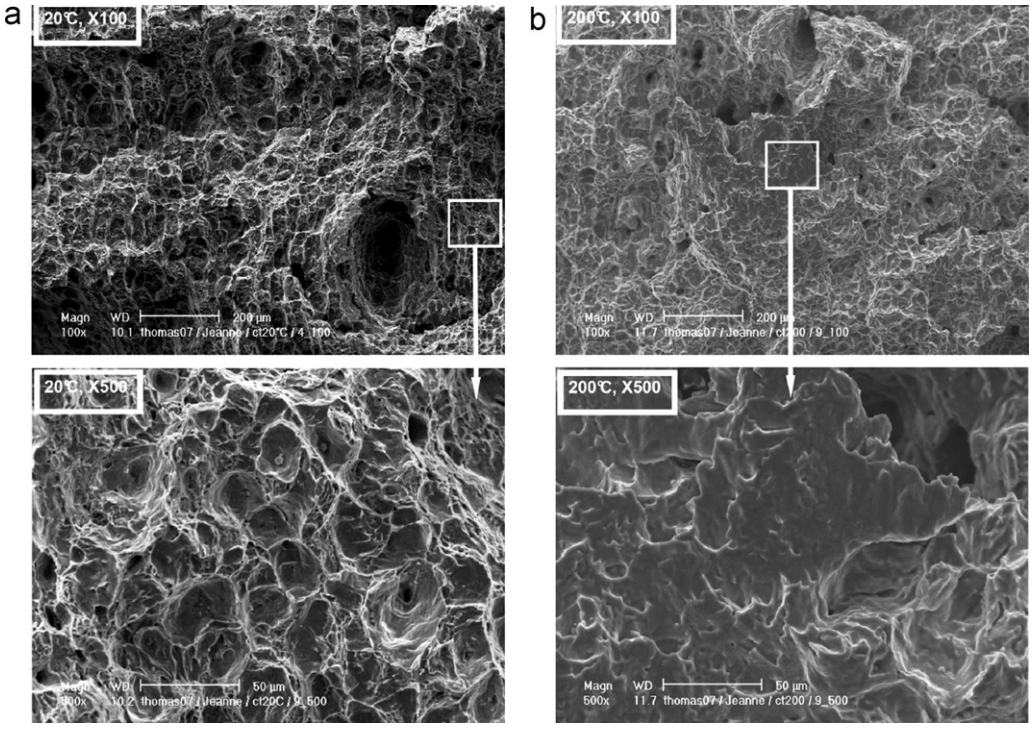

Fig. 3. Fractographic analysis of the fracture surfaces for CT specimens (a) 20 °C and (b) 200 °C: flat zones were observed at 200 °C.

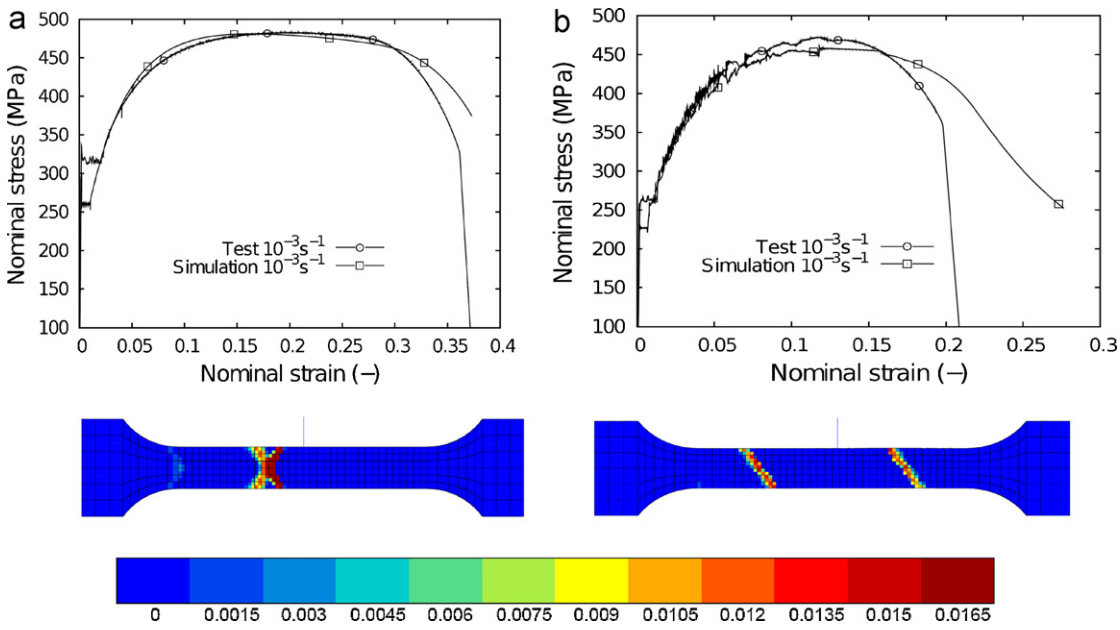

Fig. 4. Numerical and experimental tensile curves at 20 °C (a) and at 200 °C (b) at 10^{-3} s^{-1} and the corresponding strain localization bands (field of plastic strain rate).

not symmetric. Therefore, full 3D computations are necessary to correctly predict the DSA effect. The elements used were eight nodes quadratic elements with reduced integration for 2D simulations and twenty nodes quadratic brick elements with reduced integration for 3D simulations. The boundary conditions (Fig. 5) were:

1) 2D simulations: displacement equal to zero on the axis of the specimen in direction 1, displacement equal to zero on the minimum section in direction 2, and displacement rate on the upper surface in direction 2 was prescribed with details as discussed in the next paragraph.
2) 3D simulations: displacement equal to zero on the bottom surface in direction 2, displacement of one node on the bottom surface equal to zero in directions 1 and 3, displacement of the second node on the bottom surface equal to zero in direction 1 and displacement rate prescribed on the top surface in direction 2 as in 2D simulations.

Particular attention had to be paid to the prescribed displacement rate at the top of the mesh. Indeed, the actual condition in the experiment was a constant prescribed crosshead speed. This condition is not identical to a constant displacement rate at the head of the specimen (i.e. top of the mesh). The testing machine stiffness (including the grip system) modifies the displacement rate at the head of the specimen. The non-linear behavior of the specimen induces a variation of this displacement rate versus time whereas crosshead speed remains constant. Since for the DSA phenomenon, loading rate is a major concern, the displacement rate at the top of the mesh was imposed so as to obtain the experimentally-measured diameter versus time. This resulted in using three different displacement rates increasing with time (the prescribed displacement is represented in Fig. 9 by the curve entitled “node 2 without spring”). In a second step, the machine stiffness was modeled as explained in the next section.

Fig. 6 shows the results obtained from simulations and experimental for AE4 at 200 °C. Two models were used for the simulations. One is the KEMC model and the other one is a standard elasto-plastic (EP) model which does not account for strain ageing and for which the parameters were obtained from the experimental curve of the round smooth specimen tested at 200 °C and 10^{-4} s^{-1}. The results show that the global behaviors predicted by 2D and 3D computations with the KEMC model are identical: the tensile curves are superposed. However, it is also noted that the magnitude of the simulated PLC serrations are less pronounced than for the experimental curve. This is attributed to the simplified boundary conditions as discussed later in this section. The curve obtained with the EP model in 3D gives a correct simulation of the force.

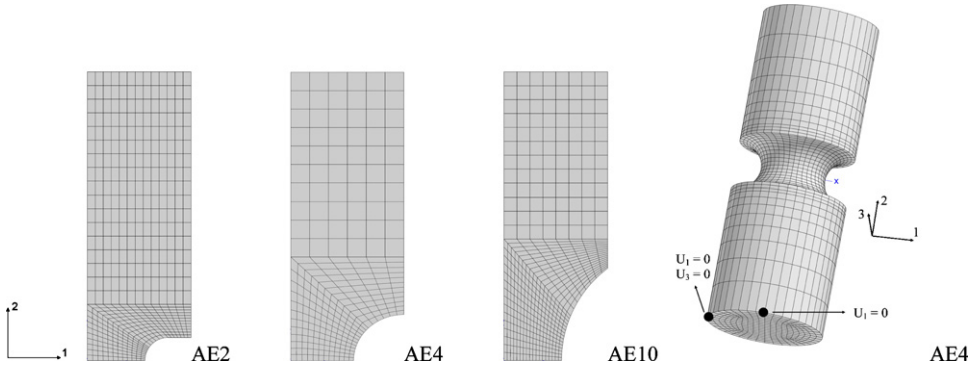

Fig. 5. Meshes of axisymmetric notched specimens.

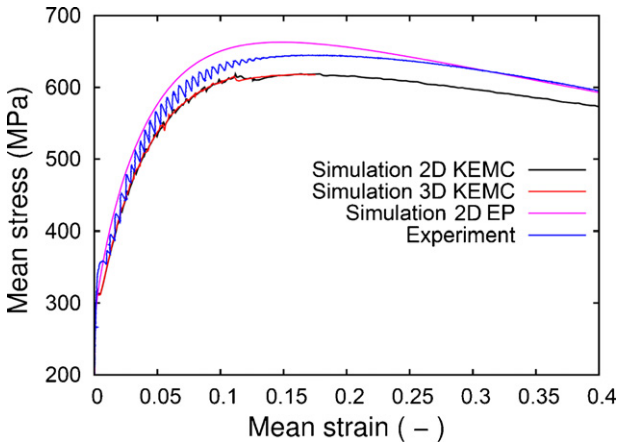

Fig. 6. Experimental and numerical curves at 200 °C: test results as well as 2D and 3D simulations for AE4.

Fig. 7 shows contour values of equivalent plastic strain rate obtained from 3D computation of AE4 at 200 °C at mean strains of 5% and 5.4%. Multiple bands develop inside the notch and are propagating. These bands occasionally extend beyond the notch region. In addition, the PLC bands on the 3D computation were not axisymmetric.

Observations of strain localization were performed by an optical technique on a mirror polished surface of the large section part of the specimen. Since strain localization can be observed in such a way only at room temperature, we looked for the Lüders bands after a tensile test interrupted during the Lüders plateau. Strain bands appear with a lattice pattern (Fig. 8). It is worth noting that the pattern observed corresponds to the pattern simulated by the FE method. Indeed, it is strain localization of DSA that is presented, but the main difference between both types of localization is the strain magnitude within the bands. Fig. 8 represents contour values of the equivalent plastic strain of simulation of the AE4 tested at 200 °C at 5% of mean strain for the two models: KEMC and EP model. Comparing the observation and the 3D-model using the KEMC constitutive law, we can conclude that the KEMC model accurately represents strain localization. Consequently, to correctly predict PLC bands on round notched specimens, 3D computations must be performed.

The boundary condition related to the prescribed displacement was modified to directly take into account the influence of the testing machine stiffness on the PLC serrations. The AE2 and AE4 specimens were simulated taking into account the testing machine stiffness by means of a layer of purely elastic elements added at the top of the meshes (Fig. 10a). These elastic elements represent the spring simulating the testing machine stiffness. Considering the testing machine and the specimen to be two elastic springs in series, the testing machine stiffness is:

$$K_m = \frac{K_t K_{sp}}{K_{sp} - K_t} \tag{6}$$

with K_t the total stiffness obtained by the ratio of the load and the crosshead displacement measured experimentally in the linear domain of behavior, and K_{sp}, the elastic stiffness of the specimen computed by finite element method (in the modeling, plane symmetry imposes to take the double of K_{sp}). The machine stiffness calculated for AE2 and of AE4 is respectively 54,878 kN/m and 55,757 kN/m. Since the global curve is not sensitive to the 2D or 3D model, 2D computations were carried out to reduce computational time. The Fig. 9 shows the constant prescribed displacement imposed to node 1 (see Fig. 10 for the definition of the nodes 1 and 2) and the resulting displacement at node 2 that varies step by step when strain localizations occur; it should be noted that this displacement fits very well the displacement prescribed at node 2 in the preliminary step of AE modeling and defined in order to recover the diameter variation of the specimen.

Fig. 10b shows simulated and experimental curves for AE2 and AE4 taking into account the testing machine stiffness. Incorporating machine stiffness into the model resulted in simulated PLC

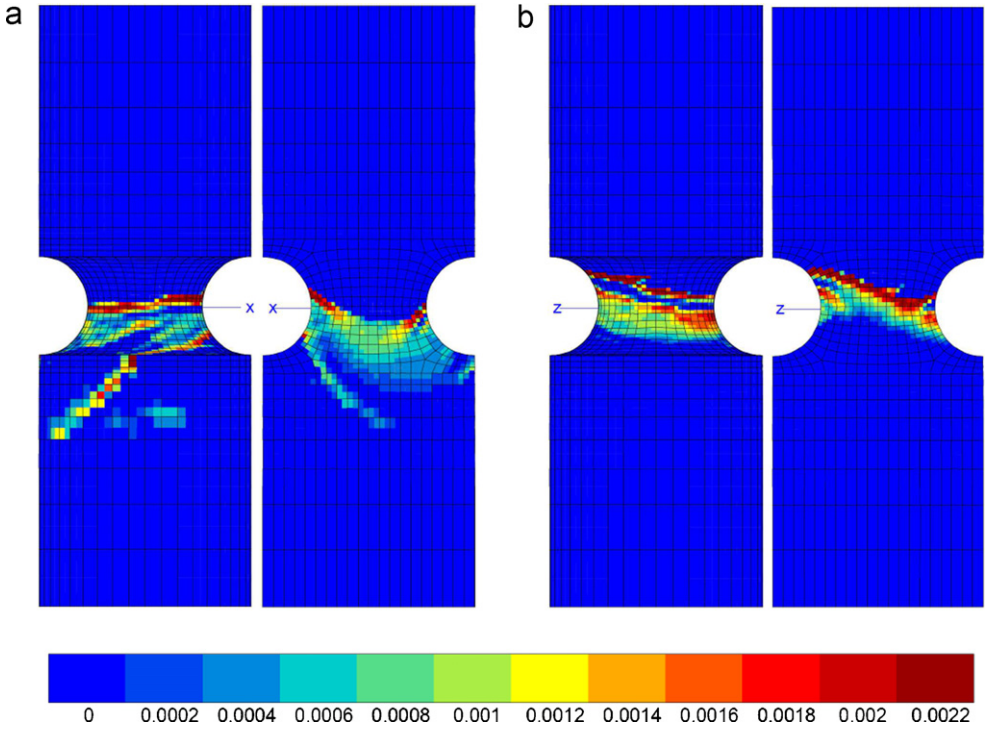

Fig. 7. Contour values of equivalent plastic strain rate ($\dot{p}$) for AE4. 3D computation using KEMC model at 200 °C for (a) 5% and (b) 5.4% mean strain: exterior surface (left) and axial section (right).

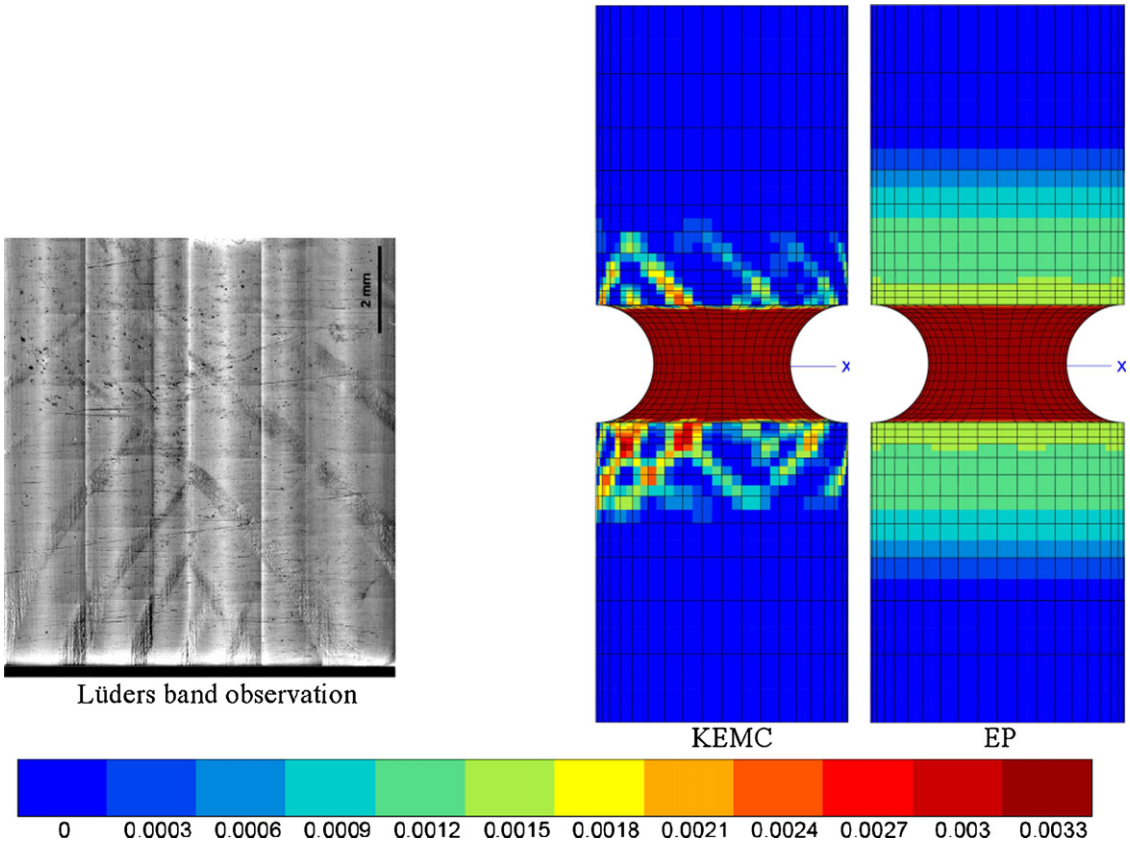

Fig. 8. Observation of the Lüders bands on specimen NT4 ahead of the notch (left), contour values of cumulative equivalent plastic strain for AE4 from 3D computations using KEMC model and EP model at 200 °C at 5% of mean strain (right).

serrations which were much closer to the experimental curves. The amplitude of PLC serrations is larger and the PLC serrations are more frequent than in the previous simulations. The larger serrations are explained by the release of elastic energy stored in the spring when strain rate localization bands form in the notch zone: since the load decreases, the displacement of the spring (*i.e.* the testing machine) decreases too, inducing a rapid increase displacement at the head of the specimen in order to reach the constant crosshead speed value that is prescribed. The local strain rate increases in the neck and a stronger PLC effect is observed. Nevertheless, it should be noted that the result could be a weaker PLC effect, if the temperature and strain rate domain is such that a higher strain rate is outside the PLC domain.

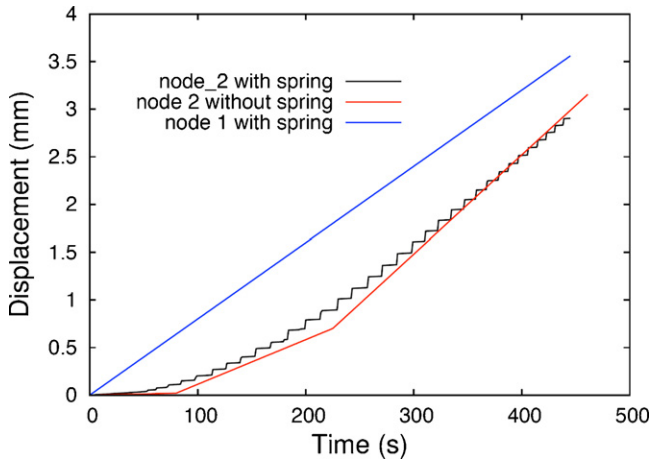

Fig. 9. Displacement of node 1 and node 2 (see Fig. 10) without or with spring.

It is also noted that the amplitude of the PLC serrations is overestimated by the simulations. This may be explained by the fact that the maximal stress drop magnitude driven by the parameter P_1 was too high. Nevertheless, it must be pointed out that such serrations were observed on experimental curves for the same type of specimens on another C–Mn steel by Wagner et al. [24]. It is worth noting that the shape of the serrations is correctly predicted. However, in contrast to the experimental results, the serrations do not stop after the maximum load indicating that the parameters controlling the solute atom concentration have to be adjusted.

These results indicated that machine stiffness should be taken into account for the identification of strain ageing parameters. This is a subtle issue that should be considered in the future because it depends on the relative stiffness between specimen and testing machine.

3.4. CT specimens

CT specimens were also simulated with the same parameters as the two preceding cases using the KEMC model. The CT specimens were firstly simulated by 2D computations since the cost of a full 3D computation is very high due to the PLC strain localizations. Full 3D computations were then carried out in order to show the geometry effect on the PLC band characteristics as was done for the notched round specimens. 2D simulations were conducted for plane stress and plane strain for later comparison with the 3D results. For saving computation time, only one half of the CT specimen was computed, even though it is known that the strain localization modes break the symmetry of specimen geometry. The element types were exactly the same as those used for the round notched specimens except

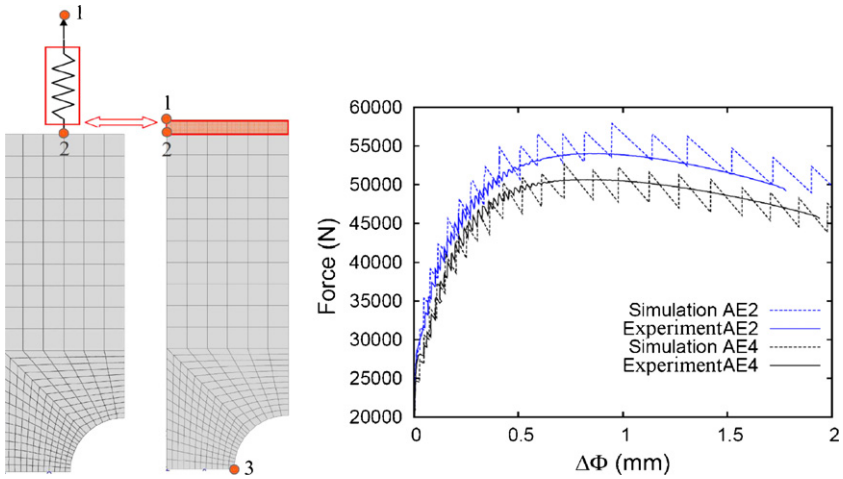

Fig. 10. (a) Mesh of AE4 with a layer of elastic elements equivalent to a spring with the same stiffness as the testing machine; and (b) simulation and experimental curves for AE2 and AE4 taking into account the testing machine stiffness at 200 °C.

that the 2D elements for CT specimens were for plane stress and plane strain state instead of for axisymmetric elements.

Fig. 11 shows the 2D mesh and the loading conditions for CT specimens. Since the machine stiffness was not taken into account in determining the material parameters, simulations were done ignoring the effect of machine stiffness. The speed prescribed to the pin loading is 0.4 mm/mn corresponding to the COD prescribed speed which was controlled by the clip gage. To simulate the experimental load, a group of elements was added to the loading hole. These elements are purely elastic with a much higher Young's modulus than the actual material, so that the elastic strain of the pin can be neglected. The loading was then applied to the tip of the elastic zone. The displacement of the tip is fixed in the direction 1 ($U_1 = 0$). Symmetric conditions were imposed on the ligament. The COD was measured at the same location as in experiments. The zone enclosed in the red box was meshed with elements of 200 μm since two types of strain localization are present in this zone: classic strain localization near the crack tip and strain localization due to the DSA effect. A sufficiently fine mesh can account for both types of strain localization. Simulations were carried out for the specimen tested at 200 °C since DSA manifested its maximum effect at this temperature: the toughness takes its minimum value.

Fig. 12a shows the field of equivalent plastic strain rate and Fig. 12b shows the cumulative equivalent plastic strain for plane stress (left) and plane strain (right) conditions at a COD of 0.73 mm.

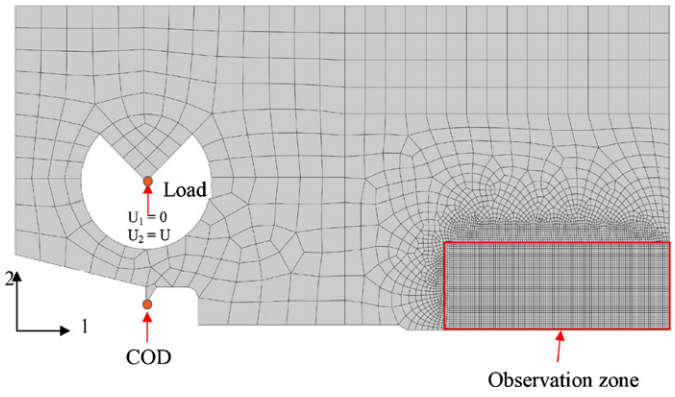

Fig. 11. 2D mesh of CT specimen.

Fig. 12a shows that, in plane stress, the PLC bands are numerous, very short and scattered near the crack tip. In plane strain, the PLC bands are much less numerous and they are much longer than those in plane stress. In Fig. 12b, it can be seen that the plastic zones are more localized compared to the classical case, i.e. with an elastic–plastic behavior [15]. In plane stress, the strain localization bands are parallel to the crack plane and similar to those observed near the notch tip of an aluminum alloy specimen by Delafosse et al. [41]. In plane strain, the plastic zone near the crack tip is localized into multiple strain bands. These strain localization bands tend to extend to the back of the specimen.

Two full 3D computations were carried out on a quarter of the whole CT25 specimen (Fig. 13) tested at 200 °C: one using the KEMC model and the other using the elastic–plastic model already presented for notched specimens. The side groove was also modeled to get a mechanical state as close as possible to the experimental situation. The loading conditions were the same as for the 2D simulations. Around the crack tip, a regular 500 μm mesh was used which was coarser than in 2D simulations owing to the increased computational time.

Fig. 14 shows the equivalent plastic strain rate at a COD of 0.7 mm for the 3D simulation with the KEMC model at 200 °C. As was the case for 2D plane strain, the PLC bands were much less numerous than those observed in 2D plane stress.

Fig. 15 shows the equivalent plastic strain at the COD of 0.7 mm for the 3D simulation with the KEMC model at 200 °C. Similar to the 2D plane strain case, the plastic zones exhibited multiple strain localization bands. These bands were also divided into two groups: one initiated from the crack tip and the other from the side groove. It is noted that the bands on the symmetry plane share the same characteristics as those simulated in 2D plane strain whereas those on the free side were less numerous and less pronounced because the material on the free side had less plastic deformation. Fig. 16 shows the equivalent plastic strain at a COD of 0.7 mm for the 3D simulation using the elastic–plastic model at 200 °C. Compared to the KEMC model, globally, the plastic zones are of the same dimension. However, the plastic zones are much less localized than those simulated with the KEMC model.

To visualize the PLC strain localization bands within the specimen, a transverse section about 5 mm from the crack tip (the length of the ligament is 20 mm) was examined (Fig. 17). For the equivalent plastic strain, the left side is the symmetry plane and the right is the free side. It is noted that the plastic zone is in the form of a half

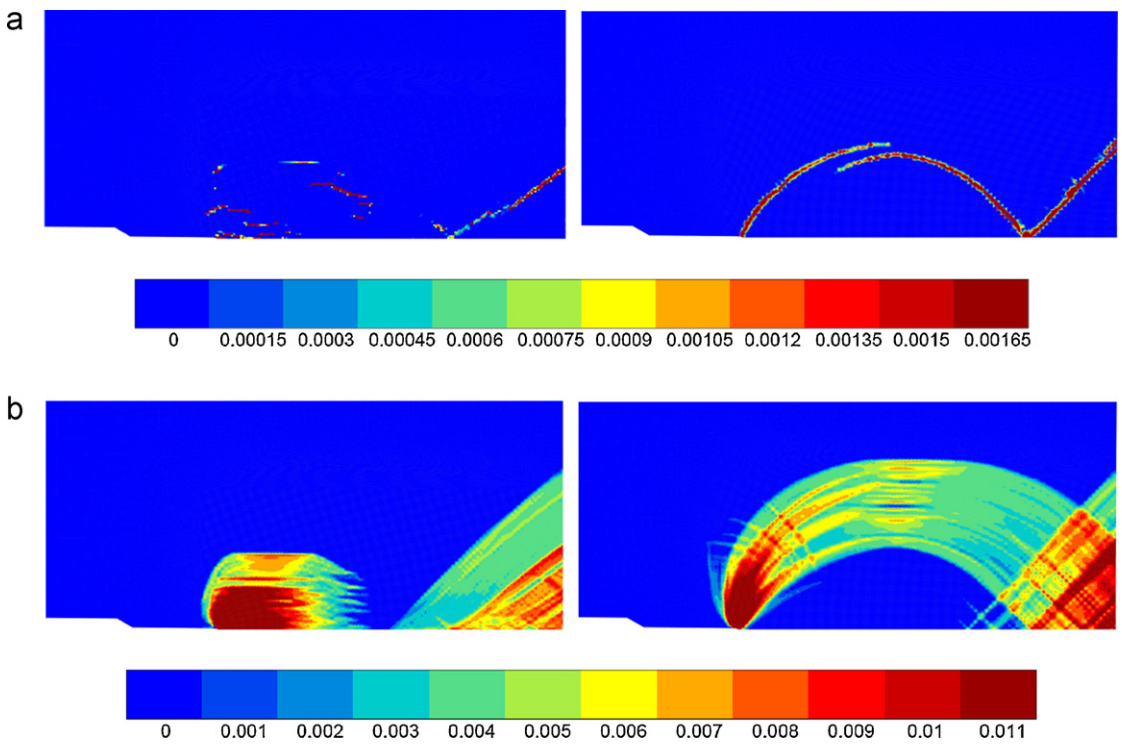

Fig. 12. Simulation results at a COD of 0.73 mm for plane stress (left) and plane strain (right): (a) field of equivalent plastic strain rate and (b) field of equivalent plastic strain.

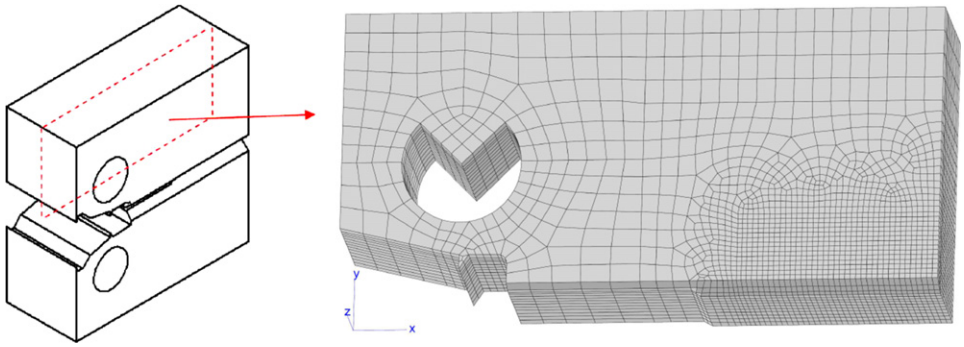

Fig. 13. Mesh of a quarter of a whole CT25 specimen.

arc which initiated from the bottom of the groove in the transverse direction. Two groups of PLC bands can be seen:

1) Bands initiated from the crack tip. These bands cross the whole specimen in the longitudinal direction (crack propagation direction) (Fig. 15).

2) Bands initiated from the groove. These bands cross the geometry in the thickness direction.

These two groups of strain localization bands interfere. Nevertheless, globally, the geometry remains in a quasi-plane strain state for ligament as it will be confirmed by the COD/force curves.

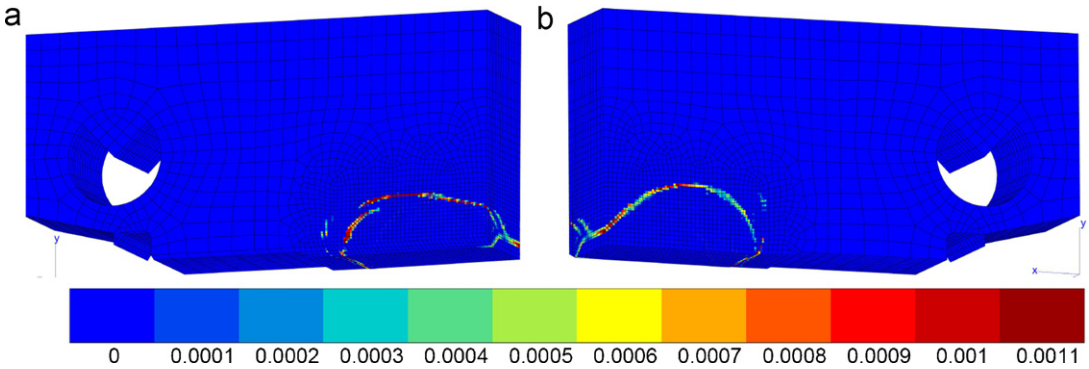

Fig. 14. Field of equivalent plastic strain rate at a COD of 0.7 mm for the 3D simulation using the KEMC model at 200 °C: (a) grooved side; and (b) symmetric plane side.

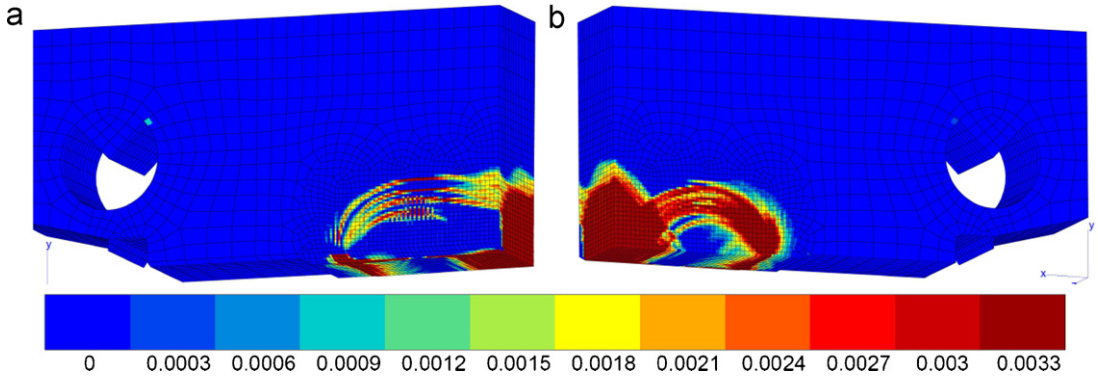

Fig. 15. Cumulative equivalent plastic strain at a COD of 0.7 mm for the 3D simulation using the KEMC model at 200 °C: (a) grooved side; and (b) symmetry plane side.

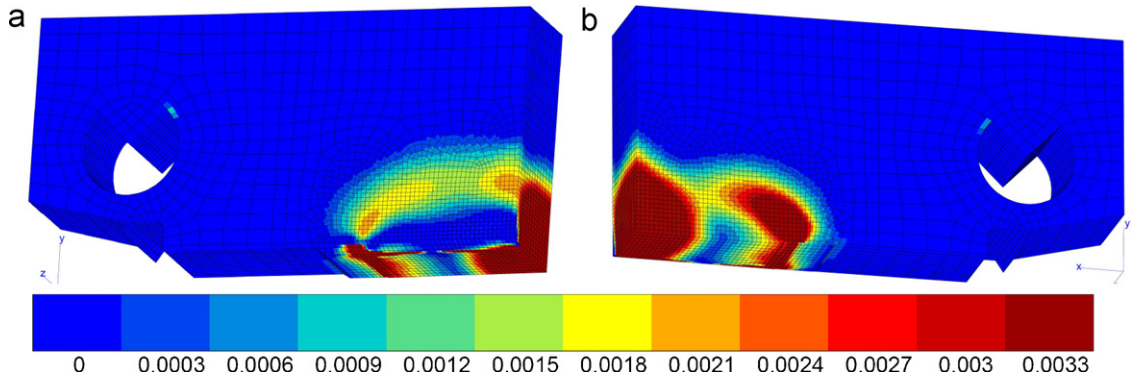

Fig. 16. Cumulative equivalent plastic strain at a COD of 0.7 mm for a 3D simulation using the elastic–plastic model at 200 °C: (a) grooved side; and (b) symmetry plane.

The 3D simulation COD/force curve was compared to those obtained from 2D simulations and to the experimental one (Fig. 18). It must be pointed out that the simulations were carried out under monotonic loading and without crack propagation. Therefore, there is no unloading line on the simulation curves and the simulated curves deviate from the experimental curve at 1.5 mm COD because of the onset of ductile tearing. Nonetheless, serrations are observed on the simulation curves which are related to the PLC effect in agreement with experiment [15]. The amplitudes of the PLC serrations obtained from simulation are higher than those seen on the experimental curve. This may be due to an over estimate of the parameter P_1. Examination of the results of the simulations shows that the plane strain 3D simulation gave the best prediction of the experimental curve. PLC serrations were also observed for the 3D simulation curve; their amplitude is lower than that of the plane strain curve and thus would appear to be more realistic. It is noted that the 3D simulation using the EP model yields results which are very close to those obtained from the KEMC 3D model even though the corresponding local strain fields are different.

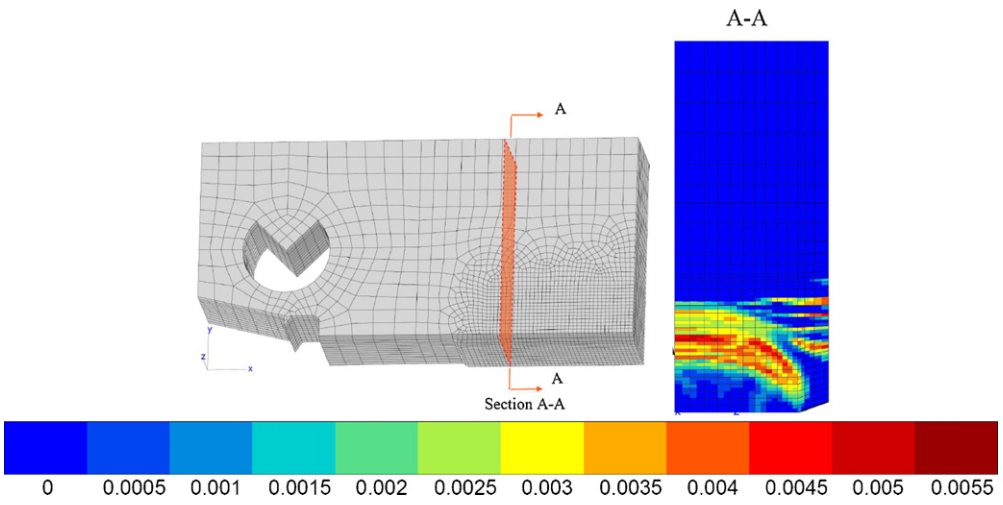

Fig. 17. Contours of cumulative equivalent plastic strain using the KEMC model at a COD of 0.8 mm: transverse section behind the crack tip.

Table 3
Parameters determined at 20 °C and at 200 °C.

Temperature (°C)	E (GPa)	N	R_0 (MPa)	Q (MPa)	b	H (MPa)	$\dot{\varepsilon}_0$ (s^{-1})	E_0 (eV)	V_a (b^3)	n	P_1 (MPa)	t_{a0} (s)	P_2 (s^{-n})	ω	α
20	210	0.3	197	312	25.2	360	1×10^{-3}	0.0022	83	0.66	94	5,000,000	0.01	0.0002	0.26
200	198	0.3	176	287	29.3	360	1×10^{-3}	0.0022	121	0.66	83	100	0.85	0.0002	0.17

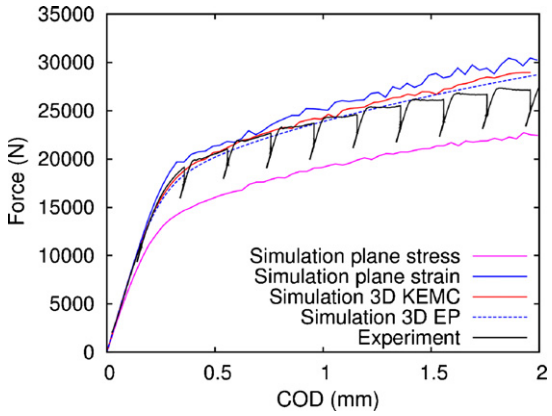

Fig. 18. Experimental and numerical force/COD curves for CT25 tested at 200 °C.

4. Ductile fracture prediction

4.1. Identification of the fracture criterion

The objective of the fracture specimen geometry modeling (notched and CT specimen) was to obtain correct mechanical fields in order to use the local approach for fracture prediction. It should be recalled that at 200 °C the ductility is lower than at room temperature. Since ductile fracture mechanisms were observed on fracture surfaces, the Rice and Tracey model was used to predict the fracture of notched specimens. The void growth ratio is computed at each point of the specimen from the Rice and Tracey damage law [29]:

$$\frac{\dot{R}}{R} = 0.238 \exp\left(\frac{3}{2}\frac{\sigma_m}{\sigma_{eq}}\right)\dot{p} \quad R(0) = R_0 \tag{7}$$

where R is the current void radius; R_0 is the initial void radius; $\dot{p}$ is the equivalent plastic strain rate; σ_m is the hydrostatic stress; σ_{eq} is the von Mises equivalent stress. Fracture is assumed to occur when the void growth ratio reaches a critical value $(R/R_0)_c$. This critical value must be determined from experiment in order to predict strain to fracture measured in experiments.

In the present study, Eq. (7) was assumed to be independent of temperature since the fractographic analysis did not show any features on the fracture surfaces uniquely associated with the DSA domain. Determination of the parameter calibration was performed at 20 °C via 2D simulations of specimen AE4. Indeed, 2D simulations proved to be sufficient for that purpose as discussed later. Fig. 19 shows the stress triaxiality ratio σ_m/σ_{eq} and the damage variable R/R_0 computed at the Gauss point that is near the specimen center versus the change in diameter at the notch section; the center of the section is the location of the largest value of the damage variable over a large variation of the diameter, and is thus the location of ductile fracture initiation. As seen in Fig. 19, the damage variable continuously increases for the KEMC model, even though there are oscillations of the local mechanical variables due to strain localizations. Indeed, the integration over time (see Eq. (7)) masks the time variations. Therefore, the damage variable assessment does not depend on symmetry, and the 2D model adequately captures the damage level, although the current variables have not the same values in the 2D and 3D computations as previously discussed. The criterion is calibrated at 20 °C in order to get the strain at fracture. The mean value obtained using the results from specimens AE4 and AE2 was $(R/R_0)_C = 2.25$.

4.2. Prediction of ductile fracture

Simulations of the notched tensile specimen AE4 were performed at each temperature, with appropriate parameter sets at

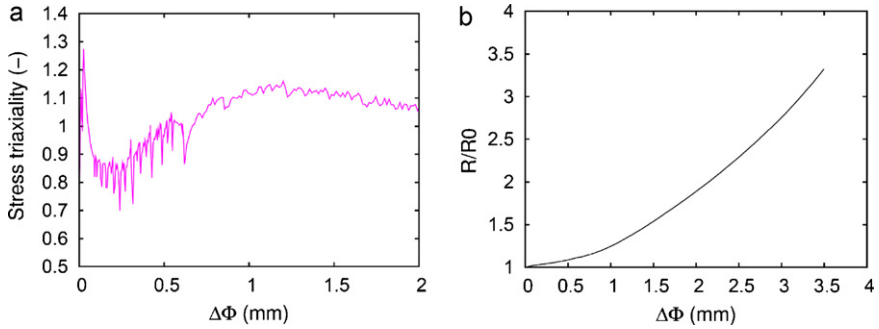

Fig. 19. Evolution of mechanical variables in the element at the center of the AE4 notched specimen; (a) stress triaxiality ratio, and (b) damage variable.

each temperature of the KEMC model. The parameter sets were not determined at each temperature. Instead the calibration procedure involved assumptions concerning the temperature dependence of each parameter as detailed elsewhere [15]. For the sake of simplicity, the results are not reproduced here and do not affect subsequent discussion. Nevertheless, it should be noted that simulation of the AE4 specimen tests underestimates the maximum load by 10% at 150 °C and 250 °C, by 5% at 300 °C, while more precise simulations are obtained for the other temperatures. These slight discrepancies underline the difficulty in predicting the correct strain rate sensitivity for DSA sensitive materials over a wide range of temperature.

Predictions of ductile fracture for AE4 were made for different temperatures (Fig. 20). As can be seen, a decrease in ductility was observed in the DSA domain in agreement with experiment. Nevertheless, the predicted magnitude of the ductility drop was less than observed experimentally. Thus, even using a model which takes the DSA effect into account, the prediction of the ductility loss at the temperature where DSA reaches its maximum effect is underestimated.

This shortcoming implies that the damage model has to be revisited. Amar and Pineau [28] and Wagner et al. [24] used the same damage model computed from an elastic–plastic constitutive law, but they assumed that the criterion was in fact temperature dependent. However they did not justify this hypothesis, and we did not observe such behavior in this study. Improved prediction of ductility loss in the negative strain rate sensitivity regime could be gained by performing micromechanical computations: particular strain hardening and strain localizations could accelerate the void growth. It should be noted that a particular attention must be paid on large strain behavior because the fracture of the AE4 specimen occurred at a local strain about 60%.

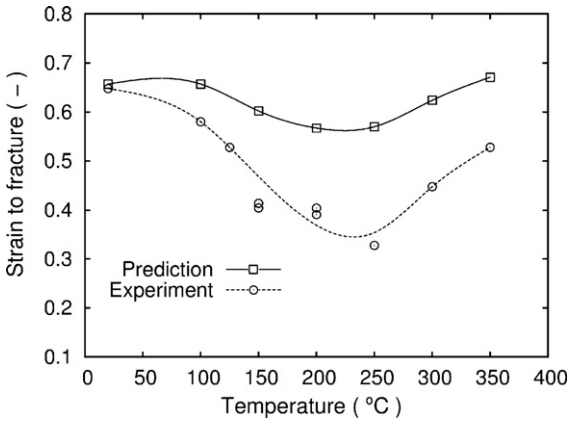

Fig. 20. Prediction of strain to fracture for AE4 from 20 °C to 350 °C.

5. Conclusions

In this study, dynamic strain ageing and its relation to ductile fracture of a C–Mn steel were studied via experimental and numerical methods.

Dynamic strain ageing was evidenced between 100 °C and 300 °C depending on the strain rate along with a decrease of the uniform elongation around 200 °C. The decreased ductility was related to the plasticity in presence of DSA which reduces the necking strain [32,33] and consequently the fracture strain. This phenomenon does not involve the relation between DSA and ductile fracture mechanisms, void nucleation, growth and coalescence.

Fracture tests were carried out on round notched and precracked specimens (CT25). A sharp drop in the fracture strain and of the fracture toughness was observed between 150 and 250 °C, a temperature range where the PLC effect was seen. Fractographic analyses by SEM did not show any feature associated with the PLC effect.

To model the fracture tests and obtain correct mechanical results in the fracture specimen, a thermally activated elasto-viscoplastic model, the KEMC (Kubin–Estrin–McCormick) strain ageing model, was used. The parameters of the KEMC model were developed between 20 °C and 350 °C from a previous work [15] and from additional results.

2D-axisymmetric and full 3D computations were then performed on round notched specimens. The results show that the global behaviors predicted by the 2D and 3D computations with the KEMC model were identical. It was noted that PLC bands in 3D computations were not symmetric. Consequently, to correctly predict PLC bands on round notched specimens, 3D computations were necessary, but were otherwise not needed to obtain the global behavior.

Fracture tests on side grooved CT specimens were also simulated. The 2D plane strain simulation was very close to the 3D simulation because of the side groove. The plastic zone had a complex spatial form due to two groups of strain bands: one coming from the crack tip and one coming from the notch of the groove. Global curves showed that PLC serrations, which were observed experimentally [15] were simulated. The global behavior of the specimen was well predicted. Since there is a high strain rate gradient in this specimen, it means that the strain rate sensitivity of the material is accurately taken into account by the KEMC model at this temperature.

The simulations with KEMC model were compared to those obtained using a standard EP model. This model accounts for the apparent strain hardening obtained from the tensile curve at 200 °C and $10^{-4}\,s^{-1}$ but which does not account for strain ageing. The global curves are reasonably predicted for the notched tensile specimen and more accurately predicted for the CT specimen at 200 °C. Indeed, this result depends on the strain rate sensitivity of the

material and on the strain rate gradient in the specimen. Thus, a prediction of mechanical behaviour of a component made for a strain ageing sensitive material with a standard elastic–plastic model is not recommended. For example, concerning the plastic zone, the lattice pattern observed on a notched specimen could not be reproduced with the plastic model. In the CT specimen, the plastic zones simulated using the KEMC model are more localized, but the plastic zone sizes are not so different.

The influence of testing machine stiffness and actual boundary conditions on PLC occurrence was assessed for the round notched specimen. The PLC serrations predicted taking testing machine stiffness into account were closer to those seen on the experimental curves. The overestimate of the PLC serrations amplitude may be explained by a too high maximal stress drop magnitude driven by the parameter P_1. Contrary to the experimental results, the serrations did not stop after the maximum load; the parameters associated with the solute atoms concentration and controlling the strain influence on free solute atoms need to be adjusted. These results indicated that machine stiffness should be taken into account for in any determination of strain ageing parameters.

Using the results obtained by the FE simulations of AE4 specimens, ductile fracture was predicted using the Rice and Tracey damage law. Based on fractographic analysis, it was assumed that the fracture criterion was independent of temperature. The ductility loss observed in the DSA domain was predicted but the magnitude was less than that obtained from experiment. Therefore, even with a model which takes the DSA effect into account for computation of mechanical parameters, the prediction of the ductility loss in the intermediate temperatures, where DSA reached its maximum effect, was still underestimated. It should be noted that the damage variable is not sensitive to the PLC effect, because it is based on the time integration of mechanical variables that masks their complex evolution. Other authors [24,28] assumed that the criterion was dependent on temperature without justifying this hypothesis. Improved prediction of ductility loss in the DSA regime could be gained by performing micromechanical computations on unit cells. Micromechanical details of strain hardening and strain localization could result in accelerated void growth.

References

[1] P. Penning, Acta Metall. 20 (1972) 1169.
[2] A. Van den Beukel, Phys. Status Solidi (A) 30 (1975) 197.
[3] L.P. Kubin, Y. Estrin, Acta Metall. 33 (1985) 397–407.
[4] K. Chihab, Y. Estrin, L.P. Kubin, J. Vergnol, Scripta Metall. 21 (1987) 203.
[5] R. Shabadi, S. Kumar, H.J. Roven, E.S. Dwarakadasa, Mater. Sci. Eng. A 364 (2004) 140.
[6] P.G. McCormick, Acta metall. 36 (1988) 3061–3067.
[7] P.G. McCormick, C.P. Ling, Acta Met. Mater. 43 (1995) 1969–1977.
[8] Y. Estrin, P.G. McCormick, Acta Met. Mater. 39 (1991) 2977–2983.
[9] P.G. McCormick, Y. Estrin, in: T.C.<ET-AL.> Lowe (Ed.), Modeling the Deformation of Crystalline Solids, TMS, Warrendale, PA, 1991, p. 293.
[10] S. Zhang, P.G. McCormick, Y. Estrin, Acta Mater. 49 (2001) 1087–1094.
[11] S. Kok, A.J. Beaudoin, D.A. Tortorelli, M. Lebyodkin, Modell. Simul. Mater. Sci. Eng. 10 (2002) 745–763.
[12] S. Kok, A.J. Beaudoin, D.A. Tortorelli, M. Lebyodkin, L. Kubin, C. Fressengeas, J. Phys. IV 105 (2003) 191–197.
[13] S. Graff, S. Forest, J.-L. Strudel, C. Prioul, P. Pilvin, J.-L. Béchade, Mater. Sci. Eng. A 387–389 (2004) 181–185.
[14] S. Graff, S. Forest, J.-L. Strudel, C. Prioul, P. Pilvin, J.-L. Béchade, Scripta Mater. 52 (2005) 1181–1186.
[15] J. Belotteau, C. Berdin, S. Forest, A. Parrot, C. Prioul, Mater. Sci. Eng. A 526 (2009) 156–165.
[16] M. Mazière, J. Besson, S. Forest, B. Tanguy, H. Chalons, F. Vogel, Comput. Methods Appl. Mech. Eng. 199 (2010) 734–754.
[17] A. Benallal, T. Berstad, T. Børvik, A.H. Clausen, O.S. Hopperstad, Eur. J. Mech. A/Solids 25 (2006) 397–424.
[18] A.H. Clausen, T. Børvik, O.S. Hopperstad, A. Benallal, Mater. Sci. Eng. A 364 (2004) 260–272.
[19] O.S. Hopperstad, T. Børvik, T. Berstad, O.-G. Lademo, A. Benallal, Modell. Simul. Mater. Sci. Eng. 15 (2007) 747–772.
[20] S.D.J. Mesarovic, J. Mech. Phys. Solids 43 (1995) 671–700.
[21] E. Rizzi, P. Hähner, Int. J. Plast. 20 (2004) 121–165.
[22] M.R. Wenman, P.R. Chard-Tuckey, Int. J. Plast. 26 (2010) 1013–1028.
[23] D. Wagner, J.C. Moreno, C. Prioul, J. Nucl. Mater. 252 (1998) 257–265.
[24] D. Wagner, J.C. Moreno, C. Prioul, J.M. Frund, B. Houssin, J. Nucl. Mater. 300 (2002) 178–191.
[25] K.C. Kim, J.T. Kim, J.I. Suk, U.H. Sung, H.K. Kwon, Nucl. Eng. Des. 228 (2004) 151–159.
[26] M. Srinivas, G. Malakondaiah, P. RamaRao, Acta Metall. Mater. 41 (4) (1993) 1301.
[27] M. Srinivas, S.V. Kamat, P. Rama Rao, Mater. Sci. Eng. A 443 (2007) 132–141.
[28] E. Amar, A. Pineau, Eng. Frac. Mech. 22 (1985) 1061–1071.
[29] J.R. Rice, D.M. Tracey, J. Mech. Phys. Sol. 17 (1969) 201.
[30] H.D. Wang, C. Berdin, M. Mazière, S. Forest, C. Prioul, A. Parrot, P. Le-Delliou, Scripta Mater. 64 (2011) 430–433.
[31] L.P. Kubin, Y. Estrin, J. Phys. III 1 (1991) 929–943.
[32] J. Kang, D.S. Wilkinson, M. Jain, J.D. Embury, A.J. Beaudoin, S. Kim, R. Mishira, A.K. Sachdev, Acta Mater. 54 (2006) 209–218.
[33] W.F. Hosford, R.M. Caddell, Metal Forming-mechanics and Metallurgy, Prentice-Hall International, Inc., 1983, 74.
[34] N. Ranc, D. Wagner, Mater. Sci. Eng. A 394 (2005) 87–95.
[35] Y. Bréchet, F. Louchet, Acta Metall. 41 (1993) 783.
[36] J.H. Yoon, B.S. Lee, Y.J. Oh, J.H. Hong, Int. J. Pres. Ves. Pip. 76 (1999) 663–670.
[37] S. Xu, X.Q. Wu, E.H. Han, W. Ke, J. Mater. Sci. 44 (2009) 2882–2889.
[38] C. Gupta, J.K. Chakravartty, S.L. Wadekar, S. Banerjee, Scripta Mater. 55 (2006) 1091–1094.
[39] C.W. Marschall, M.P. Landow, G.M. Wilkowski, ASTM STP 1074 (1990) 339–360.
[40] J. Zhang, Y. Jiang, Int. J. Plast. 21 (2005) 651–670.
[41] D. Delafosse, G. Lapasset, L.P. Kubin, Scripta Metall. Mater. 29 (1993) 1379–1384.